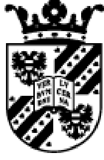

A Physically Inspired Memristor Model of the Ni/Nb:$SrTiO_3$ Schottky Interface and Its Applications

Bachelor's Project Thesis

Alina Dima, s3919951, a.dima@student.rug.nl,
Supervisors: Dr. Jelmer Borst & Thomas Tiotto, MSc

Abstract: Since the amount of data that companies and individuals use globally is increasing exponentially, processing performance should increase at the same rate. However, an exponential increase in processing power is no longer achievable due to the physical limitations of traditional computers. Neuromorphic computing represents a promising alternative because it is faster and more energy efficient. One example is brain-inspired learning using memristors, as the resistance of these devices varies based on the voltage history. Hence, they can be a natural fit for simulating synapses, whose weights vary as a function of time. The phenomenon is known as spike timing-dependent plasticity, which we aim to model. This study uses empirical data obtained from the Ni/Nb:$SrTiO_3$ Schottky interface to propose a physically plausible mathematical model. This model is then used to show that spike timing-dependent plasticity can indeed be simulated using the Ni/Nb:$SrTiO_3$ memristive device. Since synapses are at the core of brain-inspired learning and we can artificially simulate them, our study strengthens the belief that neuromorphic computing could one day replace the outdated traditional approach.

1 Introduction

The volume of data has exploded in the past decades and is predicted to continue its exponential growth, with an estimate that global data will reach 175 zettabytes by 2025 [1].

However, processing large volumes of data is becoming more difficult. Most processing units are still built using the von Neumann [2] architecture. This architecture is characterised by the separation of processing and memory, with data travelling between the two units. Since processing speed has been increasing more rapidly than memory speed, the memory wall problem became apparent [3]. This problem describes how the overall speed of the computer is slowed down due to the processor pausing while data is in the memory unit. Still, this architecture has been in use for decades because it benefited from the exponential increase of processing power described by Moore [4]. Since Moore's law is approaching its end due to physical limitations [5, 6], the feasibility of the von Neumann architecture is questioned once more. Thus, the need for a new architecture arises.

Meant to overcome the limitations of von Neumann computing, neuromorphic computing has gained popularity as an alternative approach [7, 8, 9, 10]. Inspired by computation in the human brain, the benefits of neuromorphic architectures are energy efficiency, co-located memory and processing units, parallel processing as well as an inherent ability to successfully adapt and deal with various forms of data [11, 12].

The brain is able to process data and learn through synapses, which connect the axon terminal of one neuron and the dendrites of a second neuron. The strength of the connection is linked to the action potential initiated by the presynaptic neuron and the potential spike of the postsynaptic neuron [13]. An important mechanism that determines the synaptic weights is the dependence of synaptic weights on the timing between the pre- and postsynaptic spikes [14]. This phenomenon is now known as spike timing-dependent plasticity (STDP), which has also been biologically confirmed [15].

This phenomenon has been extensively studied within the scope of neuromorphic computing

[16, 17, 18]. In these studies, STDP has been simulated using memristors. A memristor (*memory resistor*) is a passive two-terminal circuit element similar to resistors, where resistance switches between a low resistance state (LRS) and a high resistance state (HRS) depending on voltage history [19]. However, the resistance itself can take any value between the maximum value of the HRS and the minimum value of the LRS. Since both memristors and synapses are history-dependent as well as two-terminal, this makes memristors viable candidates for simulating synapses and for subsequently exhibiting STDP behaviour.

Memristors have been physically realised in 2008 [20]. Since then, different types of memristive devices, with different physical properties, have been proposed [21, 22, 23]. Some types of memristive devices need an additional electroforming step to exhibit switching behaviour [24, 25]. Thus, the focus of this study is on the less studied interface-based memristors because they possess the benefit of not requiring electroforming [23, 26].

The goal of this paper is to propose a physically plausible memristor model for the Ni/Nb:$SrTiO_3$ (Ni/Nb:STO) Schottky interface memristive device [23]. This type of memristor is of particular interest because it has not been modelled in the past and is simpler to work with due to not needing an electroforming step. A physically plausible memristor model would further bridge the gap between neuroscience and materials science, allowing neuroscientists to easily take advantage of the physical properties of memristors while simulating brain-inspired phenomena. To further stress the potential of neuromorphic computing, we aim to use our model to simulate STDP. This would provide evidence that the physical memristive device could also be able to achieve STDP behaviour.

In the next section, we will describe an existing model able to adapt to a variety of memristors, the physical properties of Ni/Nb:STO, and how STDP has been modelled in previous studies. Next, our precise methods for fitting Ni/Nb:STO devices of three radii and modelling STDP will be presented. The results, the discussion, and the conclusions will follow. The discussion will touch upon the physical plausibility of our model, which device size might be most beneficial, the outcome of STDP modelling, possible improvements, and further research.

2 Literature Review

The Yakopcic Memristor Model

One of the popular memristor models is Yakopcic's model [27]. The model can accurately fit a broad range of memristors and their characteristics. Hence, our choice is to use it as the basis of our implementation.

The model describes the current-voltage (I-V) curve as a mixture between a function h_1, which represents the HRS, and a function h_2, which represents the LRS. This can be observed in Equation (2.1), where x(t), the state variable, modulates the switch between LRS and HRS. The choice of h_1 and h_2 was specific to the type of device modelled.

$$i(t) = h_1(V(t))x(t) + h_2(V(t))(1 - x(t)) \tag{2.1}$$

The state variable changes according to Equation (2.2), where $\eta \in \{-1, 1\}$ defines the direction of the change, $g(V(t))$ implements the effect of voltage thresholds and $f(x)$ models ion motion.

$$\frac{dx}{dt} = \eta g(V(t))f(x(t)) \tag{2.2}$$

The function $g(V(t))$, as defined in Equation (2.3), is suitable for memristors that have a positive and/or negative voltage threshold. If the applied voltage $V(t)$ is between the two thresholds, the device does not change state. Otherwise, it changes according to the other two cases. The magnitudes A_p and A_n control how fast the change is.

$$g(V(t)) = \begin{cases} A_p(e^{V(t)} - e^{V_p}), & V(t) > V_p \\ -A_n(e^{-V(t)} - e^{V_n}), & V(t) < -V_n \\ 0, & -V_n \le V(t) \le V_p \end{cases} \tag{2.3}$$

The function $f(x)$ is responsible for modelling nonlinear ion motion. Ion motion influences how fast the state variable changes as it approaches either the positive boundary x_p, in Equation (2.4), or the negative boundary x_n, in Equation (2.5).

$$f(x) = \begin{cases} e^{-(x-x_p)}w_p(x, x_p), & x \ge x_p \\ 1, & x < x_p \end{cases} \tag{2.4}$$

$$f(x) = \begin{cases} e^{(x-x_n)}w_n(x, x_n), & x \leq x_n \\ 1, & x > x_n \end{cases} \tag{2.5}$$

The windowing functions w_p and w_n ensure that the state variable stays between zero and one. As a result of Equation (2.6), $f(x)$ would be zero when the state variable is equal to 1. Similarly, Equation (2.7 causes $f(x)$ to be zero when the state variable is equal to zero.

$$w_p(x, x_p) = \frac{x_p - x}{1 - x_p} + 1 \tag{2.6}$$

$$w_n(x, x_n) = \frac{x}{x_n} \tag{2.7}$$

An alternative to Equations (2.4) and (2.5) is defining nonlinear ion motion through Equations (2.8) and (2.8). The additional α_p and α_n parameters account for more variation, necessary because ion motion differs based on the device [28].

$$f(x) = \begin{cases} e^{-\alpha_p(x-x_p)}w_p(x, x_p), & x \geq x_p \\ 1, & x < x_p \end{cases} \tag{2.8}$$

$$f(x) = \begin{cases} e^{\alpha_n(x-x_n)}w_n(x, x_n), & x \leq x_n \\ 1, & x > x_n \end{cases} \tag{2.9}$$

The Ni/Nb:$SrTiO_3$ Memristor

In this paper, we aim to model the memristive device described in [23]. The memristive behaviour of this device is given by the Schottky interface of Nb-doped $SrTiO_3$ with a metal layer of Ni and Au, as illustrated in Figure 2.1.

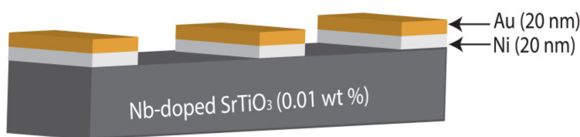

Figure 2.1: Schematic of the Ni/Nb:STO device. Adapted from [23].

In forward bias (for positive applied voltage), the current density of the device follows thermionic emission, characterised by Equation (2.10) [23],

$$J(V) = A^* T^2 e^{-\frac{q\Phi_B}{k_B T}} (e^{\frac{qV}{nk_B T}} - 1) \tag{2.10}$$

where A^* represents the Richardson constant, T the temperature, q the elementary charge, Φ_B the height of the Schottky barrier, k_B the Boltzmann constant, V the voltage and n the ideality factor. However, in reverse bias (for negative applied voltage), tunneling takes place. The effects of electron tunneling can be modelled through Equation (2.11) [29],

$$I \approx \beta \sinh(\alpha V) \tag{2.11}$$

where α and β are fitting parameters and V is the voltage. Since we did not want to assume any specific type of tunneling, we used Equation (2.11) because it is a generalised interpretation [30].

The interaction between tunneling and thermionic emission has been previously modelled through Equation (2.12) [31],

$$I = (1-w)\alpha[1 - \exp(-\beta V)] + w\gamma \sinh(\delta V) \tag{2.12}$$

where w is the internal state variable, V is the voltage, α and β are the Schottky transmission fitting parameters and γ and δ are the tunneling fitting parameters. In Equation (2.12), the first term is a simplification of Equation (2.10), whereas the second term is modelled precisely after Equation (2.11).

STDP Modelling

STDP has been modelled by applying a series of pre- and postsynaptic voltages to achieve synaptic weights that follow Equation (2.13) [32]. In this equation, Δw is the change in synaptic weight and Δt is the timing difference between the pre- and postsynaptic spikes. A_+ and A_- represent the maximum synaptic modification when $\Delta t \to 0$, whereas τ_+ and τ_- are time constants. The equation describes long term depression (LTD) when $\Delta t < 0$ and long term potentiation (LTP) when $\Delta t > 0$. Figure 2.2 provides a visual representation of Equation 2.13.

$$\Delta w = \xi(\Delta t) = \begin{cases} A_+ e^{\Delta t/\tau_+}, & \Delta t < 0 \\ -A_- e^{-\Delta t/\tau_-}, & \Delta t \geq 0 \end{cases} \tag{2.13}$$

In computational models of STDP, Δw is the change in conductance (ΔG) and has been described by Equation (2.14) [18], where G_{before} and

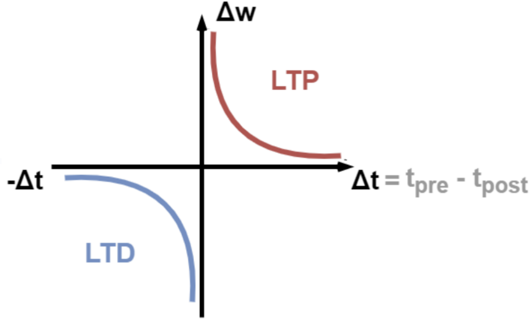

Figure 2.2: Example of standard STDP behaviour.

G_{after} are the conductances before and after the pre- and postsynaptic spikes.

$$\Delta G = \frac{G_{after} - G_{before}}{G_{before}} \cdot 100 \tag{2.14}$$

The type of spike applied to a memristor is relevant, as it influences the STDP curve. An overview of possible types of spikes is provided in [33]. The range of pre- and postsynaptic voltages is quite vast. Triangular waves, step pulses and exponential pulses are all possible options.

Additionally, to set Δt in a biologically informed manner, one can follow the proposal of Bi and Poo [15]. They experimentally showed that there is a critical 40 ms window for Δt such that it induces synaptic change.

3 Methods

Memristor Model

The model we propose is based on Yakopcic's model [27]. To model the I-V curve, change in state variable, bias thresholds and positive windowing function we still use Equations (2.1), (2.2), (2.3) and (2.6).

However, we propose Equations (3.1) and (3.2) to model h_1 and h_2, respectively. The parameters $gmin_n$, $bmin_n$, $gmax_p$ and $bmax_p$ are compact representations of the physical quantities present in Equation (2.10). Moreover, $gmin_p$, $bmin_p$, $gmax_n$ and $bmax_n$ ensure flexibility in modelling tunneling for different types of devices [28]. The h_1 and h_2 functions need to be polarity dependent, since the behaviour of our device is highly influenced by the bias [23]. Additionally, each bias is dependent on Equation (2.12) to model the interaction between tunneling and thermionic emission specific to Ni/Nb:STO. The ordering of the equations used in each bias is now arbitrary. That being said, x_0 and η will be set to appropriate values, such that the model uses more thermionic emission in forward bias and more tunneling in reverse bias.

$$h_1 = \begin{cases} gmin_p \cdot sinh(bmin_p \cdot v), & v \geq 0 \\ gmin_n \cdot (1 - e^{-bmin_n \cdot v}), & v < 0 \end{cases} \tag{3.1}$$

$$h_2 = \begin{cases} gmax_p \cdot (1 - e^{-bmax_p \cdot v}), & v \geq 0 \\ gmax_n \cdot sinh(bmax_n \cdot v), & v < 0 \end{cases} \tag{3.2}$$

To model ion motion, we will use Equations (2.8) and (2.9), as they account for more variability than Equations (2.4) and (2.5).

An overview of all equations used by this model can be observed in Table 3.1.

Parameter Tuning

The model previously described will be fit using experimental data. Such data was obtained for devices of 10 µm, 32 µm and 100 µm. Each device went through multiple voltage sweeps, for which the current was measured. Figure 3.1 is an example of an experimentally obtained I-V relation. The voltage sweep applied to all devices is plotted in Figure 3.2.

The first step was making sure that the model uses more thermionic emission in forward bias and more tunneling in reverse bias, so that it uses more h_2 in both cases. To achieve this, we set $\eta = 1$ and $x_0 = 0$. As $\eta = 1$, dx/dt will increase when a positive voltage is applied and decrease from the negative voltage.

Since the behaviour of the memristor is given by the change in state variable, fitting the model becomes solving a differential equation. The numerical method used to integrate dx/dt is fifth-order Radau IIA, implemented by the *scipy.integrate.solve_ivp* Python function. To use this method, we needed some initial state, a set of parameters that already represent a reasonable fit. Thus, we manually fitted the measurement from Figure 3.1 and used the parameter values as initial

Table 3.1: Model equations

I-V characteristic
$i(t) = h_1(V(t))x(t) + h_2(V(t))(1 - x(t))$
LRS equation
$h_1 = \begin{cases} gmin_p \cdot sinh(bmin_p \cdot v), & v \geq 0 \\ gmin_n \cdot (1 - e^{-bmin_n \cdot v}), & v < 0 \end{cases}$
HRS equation
$h_2 = \begin{cases} gmax_p \cdot (1 - e^{-bmax_p \cdot v}), & v \geq 0 \\ gmax_n \cdot sinh(bmax_n \cdot v), & v < 0 \end{cases}$
Threshold-induced state variable change
$g(V(t)) = \begin{cases} A_p(e^{V(t)} - e^{V_p}), & V(t) > V_p \\ -A_n(e^{-V(t)} - e^{V_n}), & V(t) < -V_n \\ 0, & -V_n \leq V(t) \leq V_p \end{cases}$
Nonlinear ion motion
$f(x) = \begin{cases} e^{-\alpha_p(x - x_p)} w_p(x, x_p), & x \geq x_p \\ 1, & x < x_p \end{cases}$ $f(x) = \begin{cases} e^{\alpha_n(x - x_n)} w_n(x, x_n), & x \leq x_n \\ 1, & x > x_n \end{cases}$
Windowing functions
$w_p(x, x_p) = \frac{x_p - x}{1 - x_p} + 1$ $w_n(x, x_n) = \frac{x}{x_n}$
State variable motion
$\frac{dx}{dt} = \eta g(V(t)) f(x(t))$

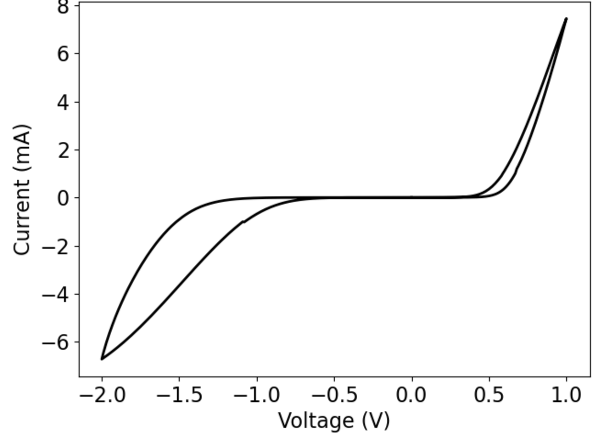

Figure 3.1: I-V characteristic for a voltage sweep applied to the 10 µm device

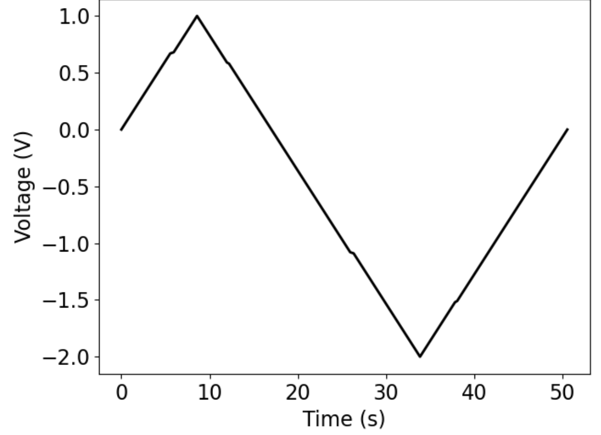

Figure 3.2: Voltage sweep applied to the model and all physical devices

estimates to fit all other measurements. The initial estimate can be seen in Table 3.2 and its resulting behaviour in Figure 3.3.

We then integrated all measurements of all device sizes using the values from Table 3.2 as the initial state. This was done to observe if any parameters appear to be constant regardless of the dimension of the device. Table 3.3 represents the parameters that we have set as constant. Since the description of the physical device does not indicate any voltage thresholds, the values of V_n and V_p have been set to 0. The other parameters set to a constant value are A_p, α_p, x_0 and x_p, as they showed almost no variation.

Then, we integrated all experimental measurements once more using the same type of Radau integration as before. This time, the constant parameters were set to the values specified in Table 3.3, while all other parameters were variable. The initial estimate for the variable parameters was the same as in Table 3.2. To get the final parameter sets, we averaged the parameters resulting from fitting the devices at the three different scales.

To assess how device radius influences the energy consumption of the memristor, we computed the energy that each memristor model uses during a voltage sweep such as the one in Figure 3.1. The energy was calculated by integrating the power, which is the voltage multiplied by the current, over time.

We used the *scipy.integrate.quad* Python function to integrate the power over time.

Parameter	Value
A_n	0.0255
A_p	0.071
V_n	0
V_p	0
α_n	1
α_p	9.2
bmin_n	6
bmin_p	5.5
bmax_n	3.13
bmax_p	0.01
gmin_n	1.05e-05
gmin_p	0.00027
gmax_n	1.95e-05
gmax_p	0.04
x_0	0
x_n	0.152
x_p	0.11

Table 3.2: Initial parameter estimate

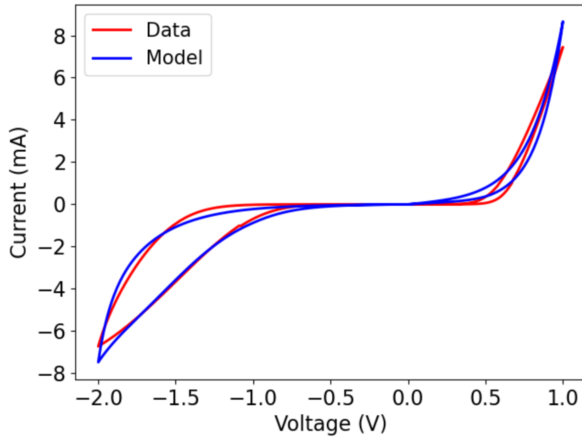

Figure 3.3: I-V curve of device from Figure 3.1 with parameters from Table 3.2

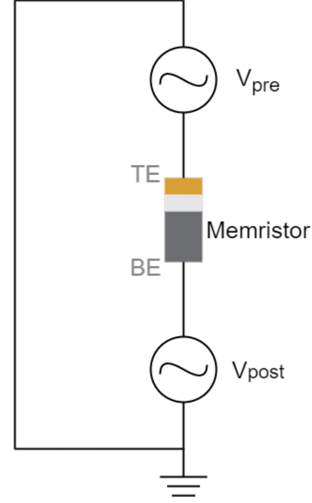

Figure 3.4: Circuit diagram of how the pre- and postsynaptic spikes have been applied to the memristor models.

Parameter	Value
A_p	0.071
V_n	0
V_p	0
α_p	9.2
x_0	0
x_p	0.11

Table 3.3: Constant parameters

STDP Model

To simulate STDP, we used the three memristor models we had previously obtained for the three different device sizes. The models were implemented in LTspice, a SPICE (Simulation Program with Integrated Circuit Emphasis) simulator. SPICE enables users to design electronic circuits and observe their behaviour by allowing them to measure various physical quantities throughout the circuits.

To each SPICE memristor model, we applied a series of presynaptic (V_{pre}) and postsynaptic (V_{post}) spikes to their top electrodes (TEs) and bottom electrodes (BEs), respectively. A visual representation of the process is provided by Figure 3.4.

The timing between the two spikes ($\Delta t = V_{pre} - V_{post}$) was set to $\Delta t \in \{-50, 50\}$ ms, since it was close to the range described by [15] as appropriate.

Figure 3.5 represents the V_{pre} we used. V_{pre} is an

adaptation of one of the spikes for which STDP was achieved in [33]. However, we set the positive pulse to 1 V and the negative pulse to -2 V, so that it is similar to Figure 3.2, for which we fitted our models. The negative peak was applied before the positive one, as the models start in HRS and we wished for the conductance to decrease with a decrease in voltage. All other parameters were manually fitted.

V_{post} was obtained similarly to V_{pre}, the difference being that its delay was 50 ms + Δt.

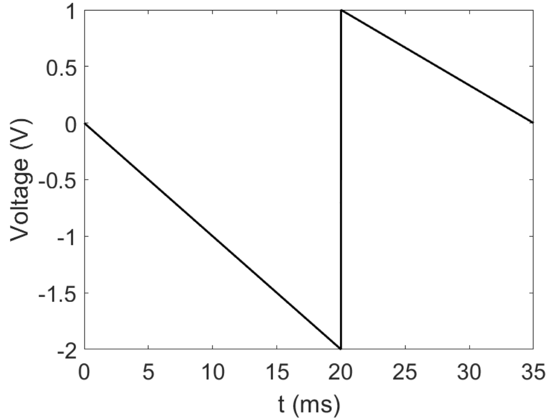

Figure 3.5: Presynaptic voltage used to simulate STDP

To measure the conductance after each set of spikes, we applied a reading voltage (V_{read}) to the top electrode of the memristor. V_{read} was a pulse of 1 V amplitude, 10 ms width and 200 ms delay. G_{after} was read at 206 ms.

Next, the conductances were normalised according to Equation (2.14), with G_{before} measured at $t = 0$ ms.

4 Results

Memristor Model

The final parameter values, alongside their standard deviations (SDs), can be consulted in Table 4.1. The values were averaged by device radius, taking into account all experimental data available. Alternatively, for a visual representation of parameter variation as a function of device radius, Figure 4.1 can be referred to. From Table 4.1 and Figure 4.1, we can infer that (1) A_n, α_n and x_n are positively correlated to device radius, (2) $gmax_p$, $bmax_p$ and $gmax_n$ are negatively correlated to device radius, and (3) $gmin_n$, $gmin_p$, $bmin_p$ and $bmin_n$ are independent of device radius.

The sets of final parameters were used to plot Figure 4.2, where each model was plotted against the corresponding averaged experimental data based on device radius. The plot indicates a positive correlation between the device radius and the magnitude of the current.

For a quantitative evaluation, we computed the relative error between the model and the averaged data for each of the three device sizes. The relative errors for the 10 µm, 32 µm and 100 µm devices were 12.45%, 11.06% and 9.37%, respectively. The mean relative error was obtained by averaging the three relative errors and is approximately 11%.

The energy consumption of the three modelled memristive devices can be observed in Figure 4.3. We can notice two convergence areas for each device: Level 1 and Level 2. Level 1 corresponds to the model switching from HRS to LRS, whereas Level 2 corresponds to the model switching from LRS to HRS. Additionally, Figure 4.3 provides an overview of energy consumption based on device radius at each level. There appears to be a positive correlation between radius and energy for both switching levels.

STDP

The results of the STDP simulation for all three device sizes were plotted in Figure 4.4. The plot represents the change in conductance as a function of the change in time. The curves that resulted follow the same overall shape regardless of radius. That is, the change in conductance decreases exponentially from zero to the absolute minimum for a negative Δt, and it decreases exponentially from the absolute maximum to zero for a positive Δt. For all device sizes, we can observe that the absolute minimum change in conductance occurs at negative zero, whereas the absolute maximum occurs at around 10 ms.

However, the radius of the memristor does cause one difference in STDP behaviour, namely the negative correlation between device size and conductance change magnitude. The magnitude decreases by about an order of magnitude as the size of the device increases.

	10 µm device		32 µm device		100 µm device	
Parameter	**Value**	**SD**	**Value**	**SD**	**Value**	**SD**
A_n	0.02662694665	1.70e-03	0.02568872249	2.40e-04	0.02428911723	1.88e-03
A_p	0.071	0	0.071	0	0.071	0
V_n	0	0	0	0	0	0
V_p	0	0	0	0	0	0
α_n	0.2786493102	3.75e-01	0.2759870683	3.84e-01	0.2497672659	2.22e-01
α_p	9.2	0	9.2	0	9.2	0
$bmin_n$	6.350156295	3.25e-01	5.787371639	1.67e-01	6.062818548	5.54e-02
$bmin_p$	4.933182609	1.40e-01	4.961102879	4.40e-01	5.187989524	9.30e-02
$bmax_n$	3.423278358	1.35e-01	2.560255673	1.52e-01	2.124988927	2.31e-02
$bmax_p$	0.002600090748	1.16e-03	0.03291352402	1.46e-02	0.06881418488	1.15e-02
$gmin_n$	8.86e-06	9.75e-07	4.51e-05	1.25e-05	3.26e-05	7.14e-06
$gmin_p$	0.0004344794763	6.43e-05	0.0006774071723	3.36e-04	0.0006158328101	9.26e-05
$gmax_n$	1.30e-05	1.27e-06	0.0003318341419	1.50e-04	0.001672677617	4.63e-05
$gmax_p$	0.0186210065	1.13e-02	0.05988630616	9.69e-03	0.08546184476	1.12e-02
x_0	0	0	0	0	0	0
x_n	0.1379470483	7.34e-03	0.1343531482	1.40e-02	0.09869126936	1.01e-02
x_p	0.11	0	0.11	0	0.11	0

Table 4.1: Parameter values and their standard deviation for the 10 µm, 32 µm and 100 µm devices

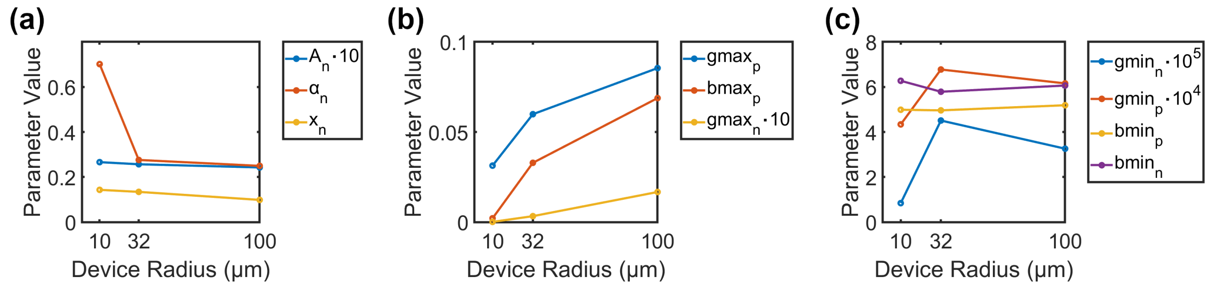

Figure 4.1: (a) A_n, α_n and x_n variation as a function of device radius. (b) $gmax_p$, $bmax_p$ and $gmax_n$ variation as a function of device radius. (c) $gmin_n$, $gmin_p$, $bmin_p$ and $bmin_n$ variation as a function of device radius.

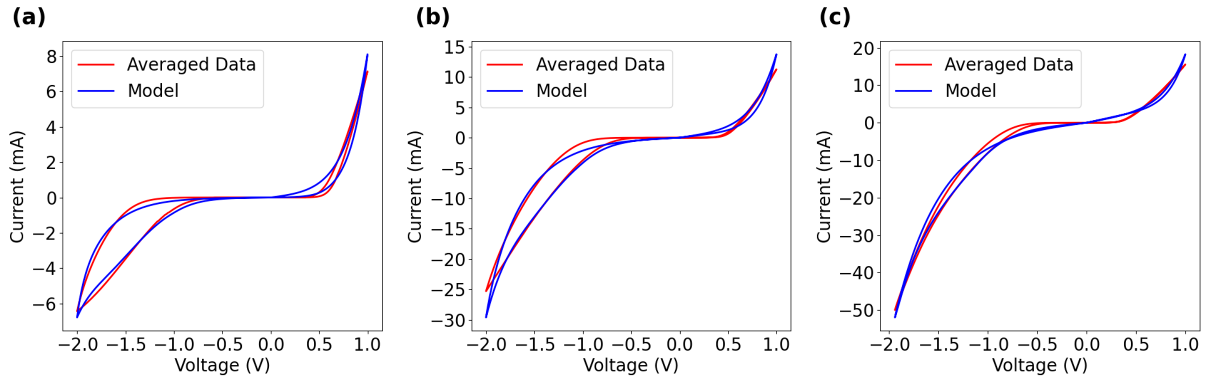

Figure 4.2: (a) I-V curve of the averaged 10 µm experimental data and the 10 µm model. (b) I-V curve of the averaged 32 µm experimental data and the 32 µm model. (c) I-V curve of the averaged 100 µm experimental data and the 100 µm model.

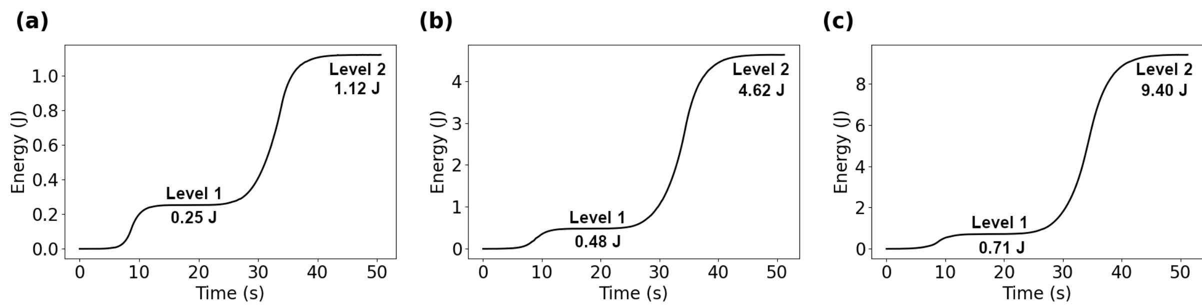

Figure 4.3: (a) Energy levels of the 10 µm model over time. (b) Energy levels of the 32 µm model over time. (c) Energy levels of the 100 µm model over time.

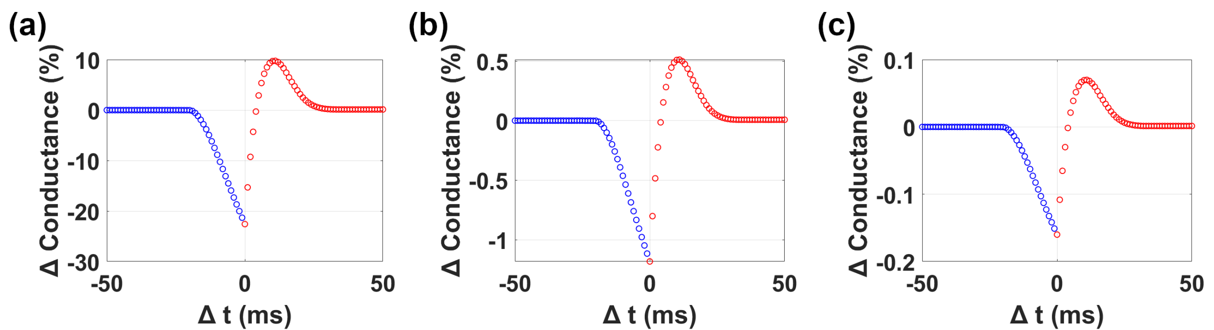

Figure 4.4: Change in conductance plotted against spike timing difference for (a) the 10 µm device, (b) the 32 µm device and (c) the 100 µm device.

5 Discussion

Since neuromorphic computing is a promising alternative [7, 8] to the current and limited computing architecture [3, 4, 5], we proposed a mathematical model for the Ni/Nb:STO memristors [23]. These memristive devices have not been modelled before, although their advantage is that they do not require electroforming. We then aimed to simulate STDP using the proposed model. Accurately simulating synapses and their properties, namely STDP in this study, presents evidence that brain-inspired learning can be artificially achieved.

Model Evaluation

Our model was optimised for Ni/Nb:STO devices of three radii, namely, 10 µm, 32 µm, and 100 µm. There appears to be a correlation between the radius and some parameters, which leads us to search for a physical interpretation.

The parameters A_n and α_n, which influence how fast the state variable changes, decrease as the radius increases. A decrease in A_n and α_n results in a smoother decrease in dx/dt. Thus, in reverse bias, larger devices result in a less abrupt drop towards using only tunneling (h_2). Because the tunneling probability is inversely proportional to the potential barrier width [30], we can hypothesise that smaller devices have a thinner potential barrier than larger devices. Similarly, the negative correlation between x_n and device radius also indicates that electrons might be able to tunnel sooner in smaller devices. A larger x_n means a higher range of x for which f decreases. This represents a quicker decrease in dx/dt for smaller devices, which was confirmed as physically plausible by Anouk Goossens during a meeting on June 27, 2022.

In forward bias, the parameters correlated to device size are $gmax_p$ and $bmax_p$. These two parameters are responsible for thermionic emission, the main effect of the forward bias. If we compare the positive side of h_2 (Equation (3.2)) to Equation (2.10), we can observe that $gmax_p$ is proportional to the height of the Schottky barrier, whereas $bmax_p$ is inversely proportional to the ideality factor. According to the same meeting with Anouk Goossens on June 27, 2022, the increase in $gmax_p$ is physically plausible, as we would expect the Schottky barrier height to increase with the size of the device. Moreover, the increase in $bmax_p$ is also physically plausible, as we would expect the ideality factor to decrease with device size. The other two parameters responsible for the forward bias are $gmin_p$ and $bmin_p$. However, considering that this effect is not representative of the positive bias, any variation in $gmin_p$ or $bmin_p$ cannot be categorically tied to any physical conclusions.

In reverse bias, the main effect is tunneling, which has $gmax_n$ and $bmax_n$ as associated parameters. The tunneling magnitude is controlled by $gmax_n$, which is proportional to the device radius. This is in accordance with the behaviour we can notice in Figure 4.2. As the device radius increases, the current that results from applying -2 V decreases. Thus, the effect has a larger magnitude. On the other hand, $bmax_n$ is inversely proportional to the radius. Normally, this would mean that tunneling magnitude would be inversely proportional to the radius. Nevertheless, this is not the case due to $gmax_n$ increasing by about an order of magnitude per device size and resulting in a more significant effect than the decrease in $bmax_n$. Although not as significant as tunneling, thermionic emission plays a role as well. The parameters describing this phenomenon are $gmin_n$ and $bmin_v$. Unlike the ($gmax_p$, $bmax_p$) pair, the ($gmin_p$, $bmin_n$) pair seems independent of radius, while being roughly constant in all three cases. We could then conclude that the Schottky barrier height and ideality factor do not vary depending on device radius in reverse bias. However, since thermionic emission is not the main effect of this bias, the outlook provided by $gmin_n$ and $bmin_n$ is not substantial.

All other parameters used by the model are constant. V_p and V_n have been both set to zero, per the physical description of the device that does not indicate the presence of voltage thresholds [23]. We have also set x_0 and η to constant values to ensure that the model uses more thermionic emission in forward bias and more tunneling in reverse bias. An exact description of the choice of x_0 and η was provided in Section 3. When it comes to A_p, α_p and x_p, one can draw a parallel with the reverse bias correspondents, A_n, α_n and x_n. In reverse bias, we concluded that smaller devices lead to a quicker change in the state variable. However, since A_p, α_p and x_p are constant, the change in state variable is not dependent on device radius in forward bias.

Figure 4.2 provides an indication that our model does qualitatively match the behaviour of the physical devices. If one wishes to decrease the 11 % mean relative error, then the model could be made less general by modifying the h_1 and h_2 functions. For example, instead of using a generalised tunneling equation like Equation (2.11), one could analyse the type of tunneling that occurs in this device and choose a more appropriate function. To improve the fit in forward bias, one could simplify Equation (2.10) less than we did in our model. However, we were not concerned with specificity, as it would result in a less generalisable model that is harder to fit and physically interpret.

The energy consumption was also calculated for all devices, as seen in Figure 4.3. We can conclude that smaller devices are more energy-efficient than larger devices, which was expected since less current flows through smaller devices (Figure 4.2). Thus, if energy efficiency is of concern, the 10 µm device is the optimal choice.

Overall, our model is physically plausible and a qualitatively good fit. Given the low amount of experimental data used during fitting, and choosing generalisability over specificity, we also managed to reach a mean relative error of only 11 %. That being said, if one application of the model would require a closer fit, then the h_1 and h_2 functions should be altered to be more specific to the physical properties of the Ni/Nb:STO device.

STDP Evaluation

The results of simulating STDP using each memristor model can be observed in Figure 4.4. To assess whether STDP was achieved, we will compare our results to the goal behaviour, Equation 2.13 and Figure 2.2. The negative side of Δt matches LTD. Additionally, the conductance for positive Δt does decrease overall, resembling LTP. Thus, we will conclude that we have achieved STDP by using the Ni/Nb:STO memristor models as artificial synapses.

However, it is worth mentioning that the LTP behaviour is somewhat atypical, as the absolute maximum change in conductance occurs at 10 ms instead of positive zero. We believe that this is caused by not fully anticipating how the model would behave on the application of $V_{pre} - V_{post}$. The atypical increase in conductance between positive zero and 10 ms might be a result of the model changing states at around 10 ms instead of zero. In the future, experimenting with different pre- and postsynaptic spikes could result in LTP behaviour that is closer to the standard.

If one wishes to focus on modelling STDP with one particular device size, we would recommend the 10 µm device. One advantage of the smaller devices is that they are more energy-efficient, as represented by Figure 4.3. Another advantage is that they show a more significant change in conductance than their larger counterparts, for which the conductance changes by less than 1% overall, as illustrated in Figure 4.4.

6 Conclusions

We proposed a mathematical model for the Ni/Nb:$SrTiO_3$ Schottky interface memristive device. The model was designed to consider the effects of tunneling and thermionic emission, which were the two phenomena regulating the behaviour of the memristor. We then optimised the model for devices of three different radii. The model proved to be physically plausible and a good fit for the physical memristive device. However, if one needs a less general model and wishes to decrease the 11% mean relative error, then the functions used to model tunneling and thermionic emission should be less general than the ones we have used.

Our trial of simulating STDP behaviour was successful but did not result in standard STDP curves. Despite achieving standard long-term depression behaviour, we were not able to obtain standard long-term potentiation. Future research could look into how this memristor model behaves during STDP simulations with different pre- and postsynaptic spikes.

This study also provided evidence that smaller devices are generally preferred, as they are more energy-efficient and lead to more significant changes in conductance during STDP simulations.

Code Availability

The code used to fit the memristor model and to implement STDP is available at `https://github.com/alina-dima/Memristor-Models`.

References

[1] D. Reinsel, J. Gantz, and J. Rydning, "The digitization of the world - from edge to core," International Data Corporation, Framingham, MA, USA, US44413318, 2018. [Online]. Available: https://www.seagate.com/files/www-content/our-story/trends/files/idc-seagate-dataage-whitepaper.pdf

[2] J. Von Neumann, "First draft of a report on the EDVAC," *IEEE Annals of the History of Computing*, vol. 15, no. 4, p. 27–75, 1993.

[3] W. A. Wulf and S. A. McKee, "Hitting the memory wall: Implications of the obvious," *ACM SIGARCH computer architecture news*, vol. 23, no. 1, pp. 20–24, 1995.

[4] G. E. Moore, "Cramming more components onto integrated circuits," *Electronics*, vol. 38, no. 8, pp. 114–117, Apr. 1965.

[5] R. Schaller, "Moore's law: past, present and future," *IEEE Spectrum*, vol. 34, no. 6, p. 52–59, 1997.

[6] L. B. Kish, "End of moore's law: thermal (noise) death of integration in micro and nano electronics," *Physics Letters A*, vol. 305, no. 3, pp. 144–149, 2002.

[7] J. Grollier, D. Querlioz, and M. D. Stiles, "Spintronic nanodevices for bioinspired computing," *Proceedings of the IEEE*, vol. 104, pp. 2024–2039, 2016.

[8] X. Yan, J. Zhao, S. Liu, Z. Zhou, Q. Liu, J. Chen, and X. yang Liu, "Memristor with ag-cluster-doped tio2 films as artificial synapse for neuroinspired computing," *Advanced Functional Materials*, vol. 28, 2018.

[9] Y. Wang, Z. Lv, J. Chen, Z.-P. Wang, Y. Zhou, L. Zhou, X. Chen, and S. Han, "Photonic synapses based on inorganic perovskite quantum dots for neuromorphic computing," *Advanced Materials*, vol. 30, 2018.

[10] N. K. Upadhyay, H. Jiang, Z. Wang, S. Asapu, Q. Xia, and J. J. Yang, "Emerging memory devices for neuromorphic computing," *Advanced Materials Technologies*, vol. 4, 2019.

[11] K. Roy, A. Jaiswal, and P. Panda, "Towards spike-based machine intelligence with neuromorphic computing," *Nature*, vol. 575, no. 7784, p. 607–617, 2019.

[12] D. Kuzum, S. Yu, and H. S. P. Wong, "Synaptic electronics: materials, devices and applications." *Nanotechnology*, vol. 24 38, p. 382001, 2013.

[13] G. J. Kress and S. Mennerick, "Action potential initiation and propagation: upstream influences on neurotransmission," *Neuroscience*, vol. 158, no. 1, pp. 211–222, 2009.

[14] W. Gerstner, R. Ritz, and J. L. Van Hemmen, "Why spikes? hebbian learning and retrieval of time-resolved excitation patterns," *Biological cybernetics*, vol. 69, no. 5, pp. 503–515, 1993.

[15] G.-Q. Bi and M.-M. Poo, "Synaptic modifications in cultured hippocampal neurons: Dependence on spike timing, synaptic strength, and postsynaptic cell type," *The Journal of Neuroscience*, vol. 18, no. 24, p. 10464–10472, 1998.

[16] S. H. Jo, T. Chang, I. Ebong, B. B. Bhadviya, P. Mazumder, and W. Lu, "Nanoscale memristor device as synapse in neuromorphic systems," *Nano Letters*, vol. 10, no. 4, p. 1297–1301, 2010.

[17] K. Seo, I. Kim, S. Jung, M. Jo, S. Park, J. Park, J. Shin, K. P. Biju, J. Kong, K. Lee, B. Lee, and H. Hwang, "Analog memory and spike-timing-dependent plasticity characteristics of a nanoscale titanium oxide bilayer resistive switching device," *Nanotechnology*, vol. 22, no. 25, p. 254023, may 2011.

[18] S. Yu, Y. Wu, R. Jeyasingh, D. Kuzum, and H.-S. P. Wong, "An electronic synapse device based on metal oxide resistive switching memory for neuromorphic computation," *IEEE Transactions on Electron Devices*, vol. 58, no. 8, p. 2729–2737, 2011.

[19] L. Chua, "Memristor-the missing circuit element," *IEEE Transactions on Circuit Theory*, vol. 18, no. 5, p. 507–519, 1971.

[20] D. B. Strukov, G. S. Snider, D. R. Stewart, and R. S. Williams, "The missing memristor found," *nature*, vol. 453, no. 7191, pp. 80–83, 2008.

[21] A. Sawa, "Resistive switching in transition metal oxides," *Materials today*, vol. 11, no. 6, pp. 28–36, 2008.

[22] R. Waser, R. Dittmann, G. Staikov, and K. Szot, "Redox-based resistive switching memories - nanoionic mechanisms, prospects, and challenges," *Advanced Materials*, vol. 21, no. 25-26, p. 2632–2663, 2009.

[23] A. S. Goossens, A. Das, and T. Banerjee, "Electric field driven memristive behavior at the schottky interface of Nb-doped SrTiO3," *Journal of Applied Physics*, vol. 124, no. 15, p. 152102, 2018.

[24] J. J. Yang, F. Miao, M. D. Pickett, D. A. A. Ohlberg, D. R. Stewart, C. N. Lau, and R. S. Williams, "The mechanism of electroforming of metal oxide memristive switches." *Nanotechnology*, vol. 20, p. 215201, 2009.

[25] J. J. Yang, D. B. Strukov, and D. R. Stewart, "Memristive devices for computing," *Nature Nanotechnology*, vol. 8, no. 1, p. 13–24, 2013.

[26] J. Rao, Z. Fan, L. Hong, S. Cheng, Q. Huang, J. Zhao, X. Xiang, E.-J. Guo, H. Guo, Z. Hou, Y. Chen, X. Lu, G. Zhou, X. Gao, and J.-M. Liu, "An electroforming-free, analog interface-type memristor based on a srfeox epitaxial heterojunction for neuromorphic computing," *Materials Today Physics*, vol. 18, p. 100392, 2021.

[27] C. Yakopcic, T. M. Taha, D. J. Mountain, T. Salter, M. J. Marinella, and M. Mclean, "Memristor model optimization based on parameter extraction from device characterization data," *IEEE Transactions on Computer-Aided Design of Integrated Circuits and Systems*, vol. 39, no. 5, p. 1084–1095, 2020.

[28] C. Yakopcic, T. M. Taha, G. Subramanyam, and R. E. Pino, "Generalized memristive device spice model and its application in circuit design," *IEEE Transactions on Computer-Aided Design of Integrated Circuits and Systems*, vol. 32, no. 8, p. 1201–1214, 2013.

[29] J. J. Yang, M. D. Pickett, X. Li, D. A. A. Ohlberg, D. R. Stewart, and R. S. Williams, "Memristive switching mechanism for metal/oxide/metal nanodevices," *Nature Nanotechnology*, vol. 3, no. 7, p. 429–433, 2008.

[30] J. G. Simmons, "Generalized formula for the electric tunnel effect between similar electrodes separated by a thin insulating film," *Journal of applied physics*, vol. 34, no. 6, pp. 1793–1803, 1963.

[31] T. Chang, S.-H. Jo, K.-H. Kim, P. Sheridan, S. Gaba, and W. Lu, "Synaptic behaviors and modeling of a metal oxide memristive device," *Applied Physics A*, vol. 102, no. 4, p. 857–863, 2011.

[32] S. Song, K. D. Miller, and L. F. Abbott, "Competitive hebbian learning through spike-timing-dependent synaptic plasticity," *Nature Neuroscience*, vol. 3, no. 9, p. 919–926, 2000.

[33] T. Serrano-Gotarredona, T. Masquelier, T. Prodromakis, G. Indiveri, and B. Linares-Barranco, "STDP and STDP variations with memristors for spiking neuromorphic learning systems," *Frontiers in neuroscience*, vol. 7, p. 2, 2013.